Journal of Renewable Materials
DOI:10.32604/jrm.2020.014158
Article

Tech Science Press

Investigation of Heterogeneous Ice Nucleation on the Micro-Cubic Structure Superhydrophobic Surface for Enhancing Icing-Delay Performance

Senyun Liu[1,2], Qinglin Liu[1,2], Xian Yi[1,2,*], Yizhou Shen[4,*], Long Guo[1,2], Wenqing Hou[4], Haifeng Chen[3] and Zhen Wang[4]

[1]State Key Laboratory of Aerodynamics, China Aerodynamics Research and Development Center, Mianyang, 621000, China
[2]Key Laboratory of Icing and Anti/De-icing, China Aerodynamics Research and Development Center, Mianyang, 621000, China
[3]Department of Materials Chemistry, Qiuzhen School, Huzhou University, Huzhou, 313000, China
[4]College of Materials Science and Technology, Nanjing University of Aeronautics and Astronautics, Nanjing, 210016, China
*Corresponding Authors: Xian Yi. Email: yixian_2000@163.com; Yizhou Shen. Email: shenyizhou@nuaa.edu.cn
Received: 04 September 2020; Accepted: 25 September 2020

Abstract: The aim of this study is to explore the heterogeneous ice nucleation behavior based on controllable micro-cubic array structure surfaces from the statistic perspective. To this end, we firstly constructed a group of micro-cubic array structures on silicon substrates by a selective plasma etching technique. After grafting low-free-energy substance, the as-constructed micro-cubic array structure surfaces exhibited higher non-wettability with the water contact angle being up to 150°. On this basis, 500 cycles of freezing and melting processes were accurately recorded to analyze the instantaneous ice nucleation behavior according to the statistical results of freezing temperature. As a consequence, the statistical freezing temperature of the sample with micro-spacing distance of 40 μm is as low as −17.13°C. This microstructure configuration (conforming to Cassie-Baxter wetting regime) not only could entrap more air pockets, but also achieved lower solid-liquid contact area, resulting in lower ice nucleation rate (~2–3 orders of magnitude less than that on the flat substrate). Furthermore, the gradually increasing micro-spacing distance to 60 μm would induce the transition from Cassie-Baxter to Wenzel wetting state, leading to higher freezing probability and ice nucleation rate. The complete understanding on microstructure configuration improving the ice nucleation will lay the foundation stone for the microstructure design of ice-repellent materials.

Keywords: Microstructure configuration; superhydrophobic; ice nucleation; anti-icing/icephobic material

1 Introduction

In recent years, the application of ice-repellent materials in the form of coatings has become the hot spot, because these materials are regarded as an ideal anti-icing or de-icing strategy without the additional energy consumption [1–4]. Generally speaking, considering the icing process, the ice-repellent materials should have greater water repellence, higher freezing delay ability, and lower ice adhesion. Among these key parameters, icing-delay ability is considered to be the core requirement, which means the response time for operating personnel to take some anti-icing or deicing actions [5–7]. As the first line of really defensing against ice accumulation, icing-delay characteristic actually refers to the freezing process, which is mainly related to ice nucleation and growth in microscopic scale. Actually, the ice nucleation and growth process completely abide the classical nucleation theory and crystal growth theory [8–10]. Water freezes after cooling, which is resulted from the decrease of Gibbs free energy. Under the thermodynamic driving force, when a sufficient number of relatively long-lived hydrogen bonds spontaneously form dense nuclei at the same position, ice nucleation will occur. Subsequently, the formed nucleus changes the shape until it reaches the stage of allowing rapid expansion, and finally leads to the crystallization of the whole system [11,12].

Taking the temperature and time into consideration, the icephobic material should have the ability to delay ice formation. Alizadeh et al. prepared a hierarchical micro-nanoscale superhydrophobic surface and systematically analyzed the transient temperature during the freezing process by a device similar to DSC (Differential Scanning Calorimetry) [13]. When the freezing event occurs, a certain amount of heat will be free, resulting in a rapid increase in instantaneous temperature. It can be clearly found from the temperature distribution that the superhydrophobic surface has lower ice nucleation temperature, which is mainly attributed to the local supercooling gradient caused by a large number of trapped air pockets inside the micro-nanoscale structures on the surface. In addition, some researchers speculated the ice nucleation behavior (such as nucleation site and direction) based on the macroscopic observation of icing process of a droplet [14,15]. Obviously, it is less rigorous and scientific to analyze the spontaneous and transient nucleation (or phase transformation) phenomenon. Also, the surface microscopic configuration undoubtedly has a significant influence on ice nucleation, because the heterogeneous ice nucleation occupies the dominant role.

Herein, we want to construct a group of micro-cubic array structures on silicon wafers by a selective plasma etching technique, and the micro-spacing distance of micro-cubic arrays is designed to induce the distinguishing non-wetting interface configurations. On this basis, the ice nucleation behaviors (including nucleation temperature and nucleation probability) are systematically investigated and discussed according to a statistic data of 500-cycle freezing temperatures. Furthermore, the ice nucleation rate is systematically calculated and analyzed based on classical nucleation theory for the complete understanding of icing nucleation and growth on the superhydrophobic surface.

2 Experimental Section

2.1 Materials and Sample Preparation

Due to the great processing performance by means of plasma etching, silicon wafers were used to construct microstructures as substrates. At first, the substrate was processed into a square plate of 20 × 20 mm^2. For other relevant reagents, the analytical grade ethanol, SU-8 photoresist, photoresist developer, and the commercial grade Heptadecafluoro-1,1,2,2-tetradecyl (FAS-17) were supplied from Sinopharm Chemical Reagent Co., Ltd., China. In the whole experiment, ultra-pure deionized water was generated by Ulupure-II-20T water system in our laboratory. Additionally, the mask used in lithography process was customized by Rigorous Technology Co., Ltd, China.

A series of micro-spacing distance *Sm*s (between two micro-columns), varied from 30 μm to 130 μm, was designed to systematically explore the heterogeneous ice nucleation behavior. The edge length of the micro-cubes was customized to be same as the height value of 20 μm. Firstly, the ethanol and deionized water were used to ultrasonically clean the samples alternately for 10 min, and the samples were dried in an oven, as illustrated in Fig. 1. Then, a layer of SU-8 photoresist with a thickness of about 5 μm was covered on the cleaned substrate sample. Subsequently, the mask template with the designed pattern was hung over the top of the photoresist layer. On this basis, the formed setup was irradiated by an ultraviolet light for 5–10 s. After successfully transferring the pattern to the sample surface, these samples were put in nitrogen atmospheric plasma etching equipment (Suzhou, China) to selectively produce the micro-cubic array structures. The plasma was generated by an AC power supply (~60 kHz) in gas flow (8 L/min), and the discharge power was about 3.0 W. The flow rate of nitrogen was controlled at 10.0 slm by the mass flow controller (MFC). After the nitrogen was applied, the plasma jets with diameters of ~4 mm and ~15 mm were generated, and the plasma etching treatment was completed within 50 s. Finally, the samples were immersed in 1 wt% FAS-17 ethanol solution for 24 h and then dried in an oven at 120°C for 2 h to obtain the excellent non-wettability.

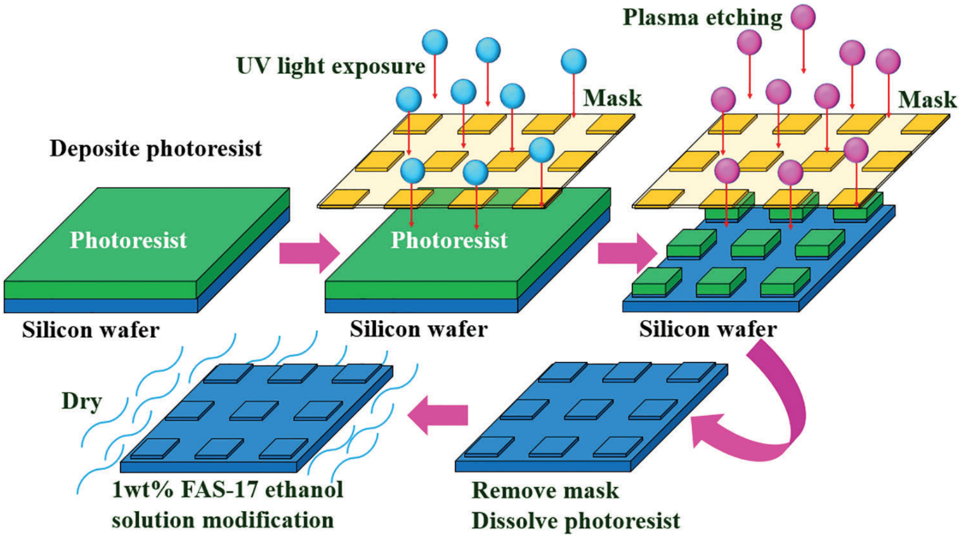

Figure 1: Schematic diagram to construct the micro-cubic array structure surface by means of a selective plasma etching method

2.2 Characterizations and Non-Wettability

The field emission scanning electron microscopy (FE-SEM; Hitachi S4800, Japan) was utilized to characterize the sample surface morphology. Furthermore, we utilized X-ray electron spectrometer (XPS; AXIS UltraDLD, Kratos, Japan) to analyze the chemical composition of the sample surface. The non-wettability of the prefabricated samples was characterized with water contact angle (WCA), which was measured directly by a contact angle analyzer (Kruss DSA100, Germany). For all samples, at least five repetitions of this measurement were performed at independent positions. Then all values were statistically averaged to ensure the accuracy of data.

2.3 Statistical Test on Freezing Temperatures

The droplet icing/melting cycles were carried out using a dedicated automatic measurement equipment, as shown in Fig. 2a. This device was composed of the thermoelectric cooling unit with loop control system and an Aluminum block (including an embedded digital temperature sensor). The cooling unit on the bottom stage was used to control the refrigeration and heating circulation system effectively. The whole chamber was made of Aluminum to diffuse the heat generated from wire and circuits. Laser was used to detect the icing events, i.e., the phase change process, where the detector was perpendicular to the laser, both pointing to the 10 μL distilled water droplet. The droplet and the sample surface were cooled from 20°C to 0°C at the rate of 20°C /min and held for 30 s, and then cooled from 0°C to −25°C with 5°C/min speed and held for 30 s to ensure the equilibrium state. After droplet completely freezing, the ice droplet was heated up to 20°C and held for 30 s to stabilize the droplet before the next cycle. The droplet icing/melting 500 cycles were performed on each sample surface. During the experiment, the temperature could be accurately recorded, as shown in Fig. 2b. Combining with the change of laser single, we could easily find the phase-changing temperature of the water droplet.

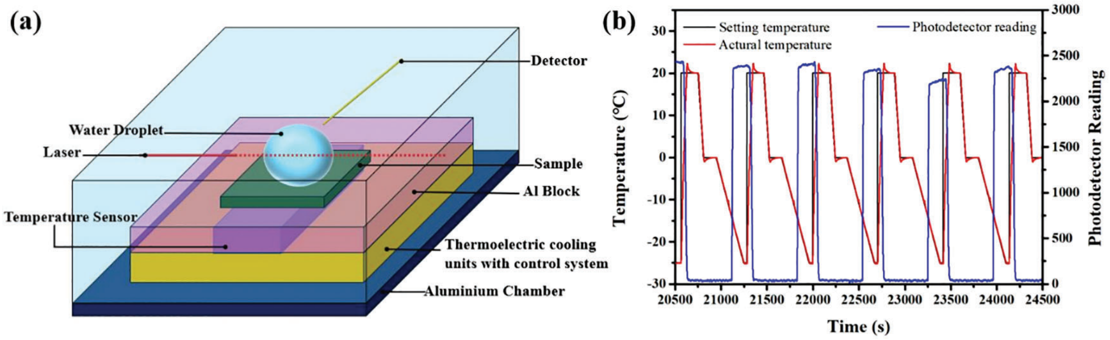

Figure 2: (a) Schematic diagram of the dedicated automatic measurement device; (b) The temperature profile of a water droplet on the surface of Sample 7 from 31th to 36th cycle

2.4 Molecular Dynamics Simulation

The ice nucleation and growth processes were simulated to further discuss the heterogeneous nucleation behavior *via* molecular dynamics simulation. In this process, the FCC surface was used as the substrate material, and the specific data is listed in Tab. 1. The subsurface diameter, the height of independent nanocubes and the distance between two nanocubes were set as 3.2 nm, 1.2 nm and 1.6 nm, respectively.

Table 1: Summary of simulation parameters of the substrate and the water-substrate interaction parameters

Surface	A_{fcc} ($\dot{A}$)	ϵ_{ws} $(kcal/mol)$	$\sigma_{ws}(\dot{A})$
FCC (100)	3.649	0.43	2.488

The sequence parameter q6 was used to identify ice and water, where the cutoff value with 0.65 was an excellent standard to distinguish between ice and liquid water [16,17]. In the cooling stage, the temperature was set to change from 290 K to 180 K with cooling rate of 1 K/ns [18]. In NVT ensemble, simulation was adopted with a time step of 10 fs, and further integrated with velocity Verlet algorithm. For every system, 5 repetition simulations were run to lessen the deviation.

3 Results and Discussion

3.1 Surface Morphology and Chemical Composition

Surface functions are mainly depended on the microscopic structures and chemical compositions, and the as-constructed microstructures illustrate complete and controllable morphologies, as shown in Fig. 3. Under the control of process parameters, the formed micro-cubic structures, fabricated by the selective plasma etching methods, evenly distribute on the substrate surface. Also, they exhibit the great cyclical features, and are belled as Sample 1–7 with the gradual increase of micro-spacing distance from 30 μm to 130 μm, (such as Sample 1: 30 μm, Sample 2: 40 μm, Sample 3: 50 μm, Sample 4: 60 μm, Sample 5: 70 μm, Sample 6: 100 μm, and Sample 7: 130 μm), respectively. Furthermore, the single microscale cubic column was designed with the side length of 20 μm, as illustrated in Figs. 3h and 3i. These geometrical parameters are considered to produce a certain effect on the interfacial wetting regime, and finally lead to the corresponding change of ice nucleation behaviors on the sample surfaces. On this basis, a surface chemical treatment is needed to regulate the surface free energy, and further achieve the special surface functions, i.e., hydrophobicity or superhydrophobicity.

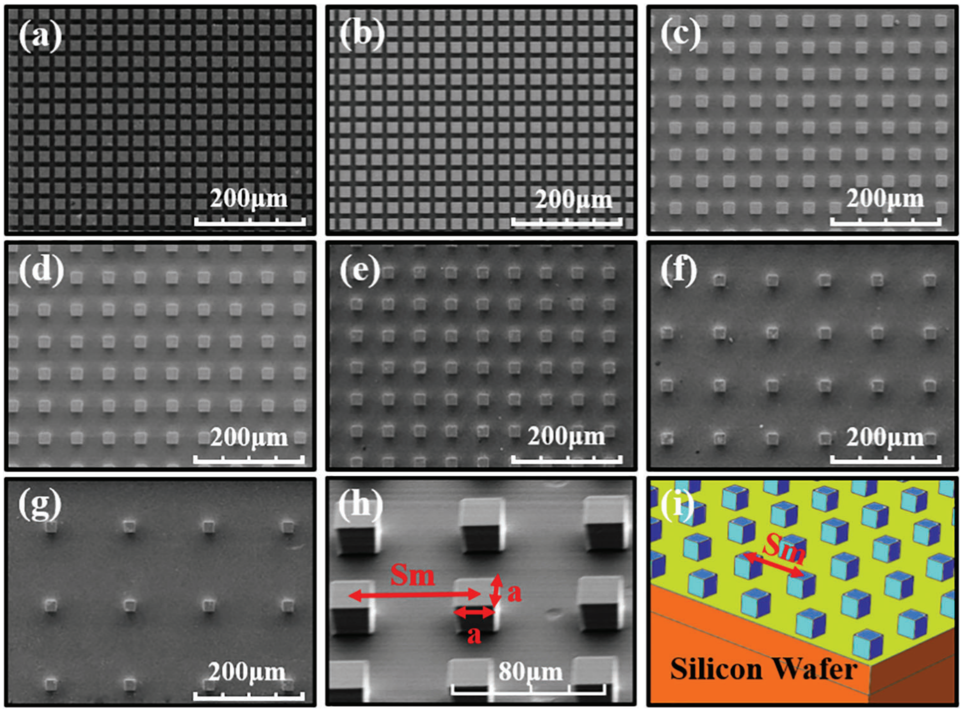

Figure 3: SEM images of micro-cubic array structures, whose center-center micro-spacing distances are (a) 30 μm, (b) 40 μm, (c) 50 μm, (d) 60 μm, (e) 70 μm, (f) 100 μm, and (j) 130 μm. (h and i) SEM images showing the morphologies of a single microscale cubic column with side length *a* of 20 μm

The chemical composition analysis was carried out on the surfaces of these samples to verify the modification of low-free-energy substance. On the basis of XPS measurement results, as shown in Fig. 4a, after low-free-energy modification, the F1s, C1s, and O1s peaks are clearly seen at the positions of 685.7 eV, 285.0 eV, and 531.8 eV, respectively [19]. In the high-resolution spectrum of F1s peak, the two peaks appear at 686.5e V and 688.9 eV, which are attributed to -CF_3 and -CF_2 [20,21], respectively, as illustrated in Fig. 4b. Analogously, in C1s and O1s high-resolution spectrums, there are many small peaks, as shown in Figs. 4c and 4d. Generally speaking, these XPS analyses can well prove that the low-free-energy groups from FAS-17 have been successfully grafted onto the prepared microstructures of sample surface, resulting in great superhydrophobicity.

3.2 Non-Wettability

The superhydrophobicity can be well reflected by the WCA paramters, and the WCAs at room temperature (20°C) and −15°C were measured by a contact angle analyzer, as listed in Tab. 2. All tested results were averaged with five test values in this work.

All these sample surfaces display the great superhydrophobicity except Sample 7 with larger *Sm* of 130 μm, because the micro-cubic structures with *Sm* of 130 μm cannot hold up the water droplet without air pockets at the solid-liquid interface, i.e., Wenzel wetting model, leading to the WCA being only 118.14°. The water droplets on the other sample surfaces (i.e., Sample 1–6) well conform to Cassie-Baxter wetting regime, and the trapped air pockets can well hold up the droplets. However, the low-temperature environment induces the contraction of air pockets to a certain extent, resulting in the reduction in WCA (such as, the value from 153.47° to 122.48° on the Sample 3 surface). At the interface aspect, the wetting regime will change from Cassie-Baxter wetting model to Wenzel wetting model or transitional wetting model.

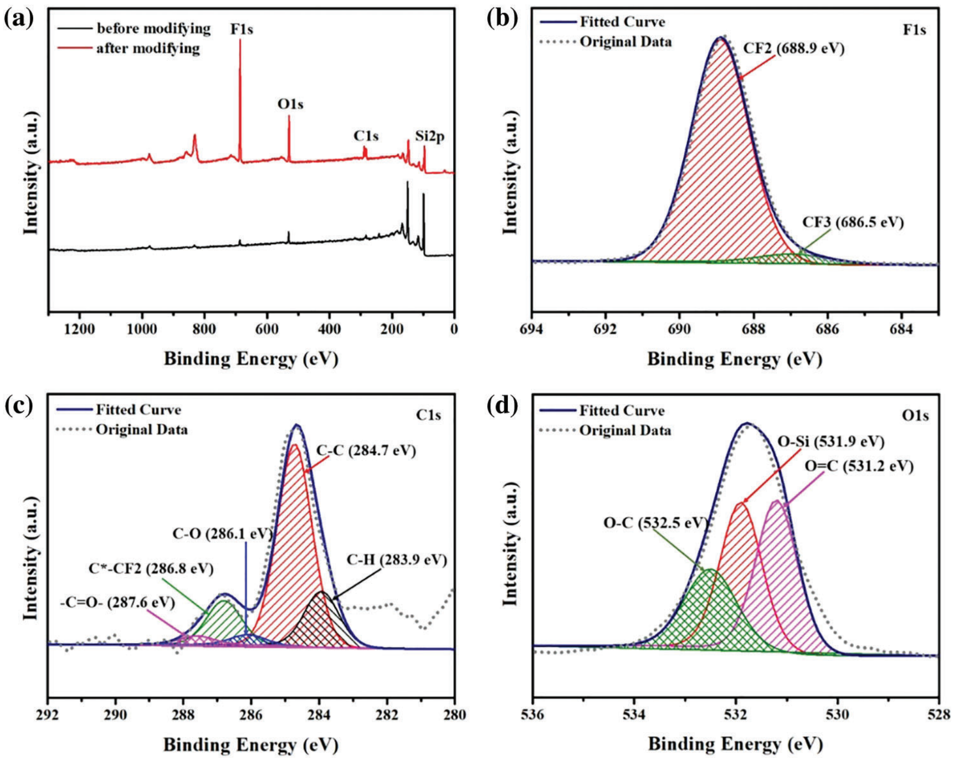

Figure 4: (a) XPS survey spectrum of the sample surface before and after the low-free-energy modification; (b and c) High-resolution spectrum of the F1s, C1s, and O1s on the modified sample surfaces

Table 2: The WCAs of a series of sample surfaces

Samples	Sample 1	Sample 2	Sample 3	Sample 4	Sample 5	Sample 6	Sample 7
WCA at 20°C	147.27° ± 2.4°	149.09° ± 1.2°	153.47° ± 1.2°	154.22° ± 1.5°	149.61° ± 1.6°	148.33° ± 1.5°	118.14° ± 1.2°
WCA at −15°C	130.75° ± 2.4°	126.07° ± 1.6°	122.48° ± 1.6°	116.35° ± 1.8°	118.22° ± 1.7°	112.00° ± 1.3°	115.32° ± 1.5°

3.3 Ice Nucleation Behavior

Subsequently, icing behavior on these as-prepared sample surfaces is discussed and analyzed in details with the statistical data of 500-cycle freezing temperatures with reference droplets, as shown in Figs. 5a–5g. It can be easily found that the freezing temperature exhibits a gradually increasing trend with raising number of icing/melting cycles, especially on the surfaces of Sample 3–6. Also, on Sample 6 surface, the freezing temperature changes more rapidly from −18°C to −12°C during the first 20 icing/melting cycles. We believe that the Cassie-Baxter wetting state is not stable for the surfaces of Sample 3–6, and the continuous icing/melting conditions can easily induce the change of interface wetting regime to Wenzel wetting model, as shown in insets of Figs. 5c–5f. Furthermore, the non-stability of Cassie-Baxter wetting state is mainly depended on the micro-spacing distance of micro-cubic structures [22,23], which well explains the rapid change of freezing temperature on the surface of Sample 6 during the first 20 icing/melting cycles. As for Sample 7 surface, the stable Wenzel wetting state belonging to the completelyinfiltrating contact type exhibits higher stability during the overall icing/melting cycles. The freezing temperature keeps relatively stable at the value of ~−13.5°C. Furthermore, there are almost no change for the freezing temperatures of reference droplets on the surfaces of Sample 1 and 2. In the two case, the micro-cubic structures with lower *Sm*s of 30 μm and 40 μm result in a stable Cassie-Baxter wetting state, which can resist the icing/melting conditions [24,25].

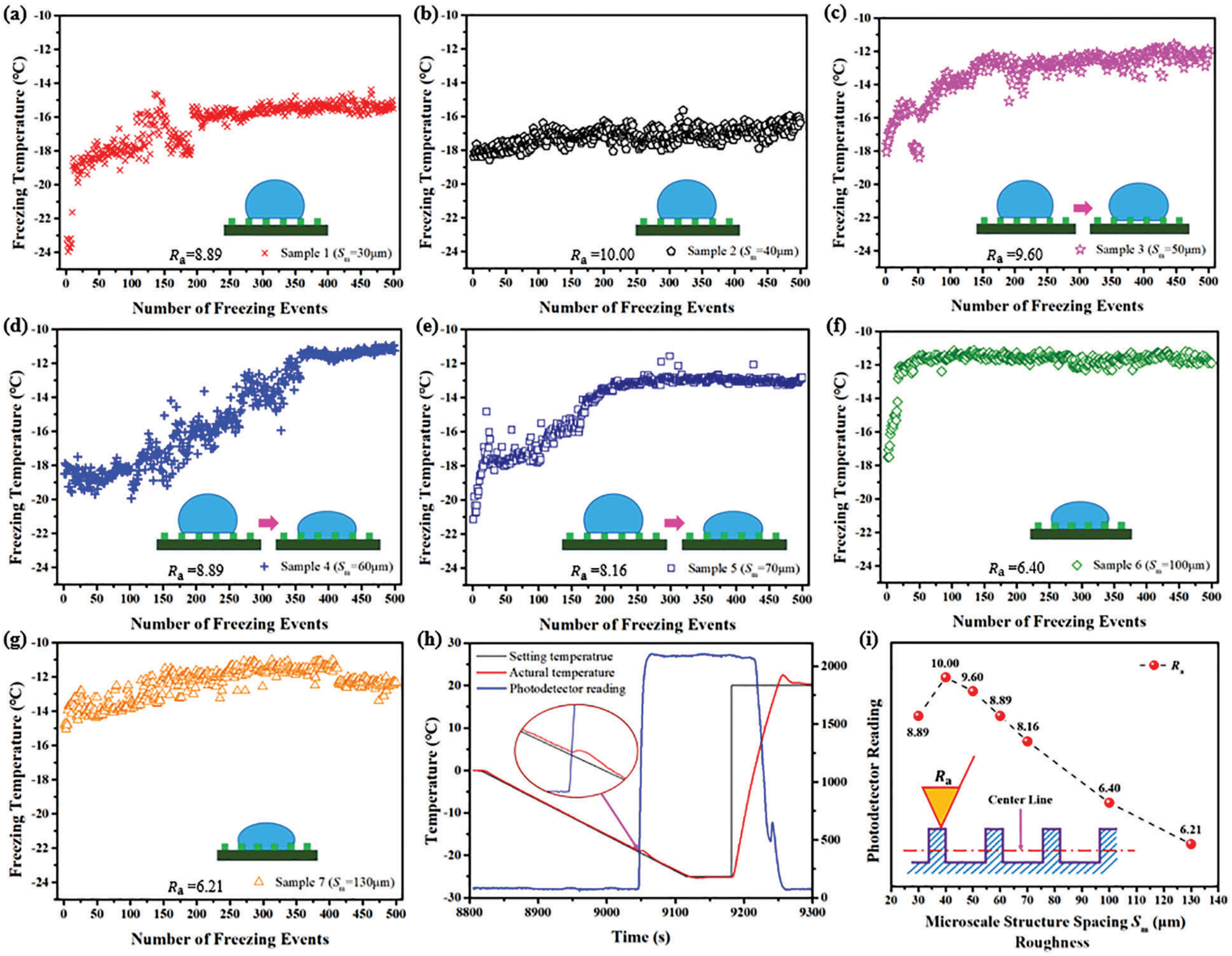

Figure 5: Statistical data of freezing temperatures of water droplets on (a) Sample 1, (b) Sample 2, (c) Sample 3, (d) Sample 4, (e) Sample 5, (f) Sample 6, and (g) Sample 7. (h) Detection of phase change from water to ice for the measurement of freezing temperature during a typical cycle on Sample 1. (i) Schematic diagram of surface roughness

Up to now, although the statistical data of 500-cycle freezing temperatures have some non-stable features, the micro-cubic structures with gradually increasing *Sm* can well explain the overall change trend of freezing temperature. As for Sample 1 and 2, the freezing temperature on Sample 2 is lower than that on Sample 1, which should be attributed to the roughness Ra, as shown in Fig. 5i. Because both of them belong to the Cassie-Baxter wetting state, the roughness will take the leading role. As a consequence, Sample 2 with *Sm* of 40 μm leads to lower solid-liquid contact area, and has greater difficulty to take place the freezing events [26–30], causing lower freezing temperature of ~−17.5°C. For the other samples (i.e., Sample 3–7) with longer *Sm*s, the wetting regime will partly or completely transfer into Wenzel wetting state, producing larger solid-liquid contact area. Consequently, there are higher freezing temperatures from −14°C to −12°C comparing with those on Sample 1 and 2. The similar experimental phenomena were reported in previous literatures [31–33].

The obtained statistical data were re-arranged to investigate the ice nucleation behavior. In the whole scanning temperature varying from 20°C to −25°C, the bin width is set as 0.2°C to discuss the freezing probability P, which is defined as [11]:

$$P = \frac{N_i}{N_0} \tag{1}$$

Among them, N_i is the number of freezing events in the i_{th} bin and N_0 is the total number of freezing events, i.e., which is 500 in this work. The freezing probability varies with temperature with Gaussian distribution, as illustrated in Fig. 6. This directly indicates that the maximum freezing probability can be generated at a certain temperature, which is not a lower value that tends to freeze on the surface of the sample. The normalized distribution equation is given by [34]:

$$P = a_1 \times e^{-\frac{(x-\mu_1)^2}{\sigma_1{}^2}} \tag{2}$$

where μ_1 is the expectation temperature, a_1 is the fitting coefficient, and $\sigma_1{}^2$ is the square diviation. The expectation temperatures of these samples can be calculated as −15.57°C, −17.13°C, −12.52°C, −11.37°C, −12.99°C, −11.57°C, and −11.88°C, respectively. For Sample 1 and 2, it means that higher supercooling degree is needed to induce the occurrence of ice nucleation, resulting in lower expectation temperatures of −15.57°C and −17.13°C for the maximum freezing probability. This is due to the stable Cassie-Baxter wetting state caused by the micro-cubic structures with lower *Sm*s of 30 μm and 40 μm. However, the micro-cubic structures with larger *Sm* (i.e., Sample 3–6) cannot well maintain the formed Cassie-Baxter wetting state, which easily transfers into the Wenzel wetting state. As a consequence, the expectation temperatures to induce the maximum freezing probability almost keep the equal level to the value for Sample 7, where the original wetting regime belongs to the Wenzel wetting state. It should be noted that the volume of reference droplet has been smaller due to evaporation as the time goes, and smaller droplet will cause the higher temperature for the occurrence of ice nucleation or the maximum freezing probability [35–37].

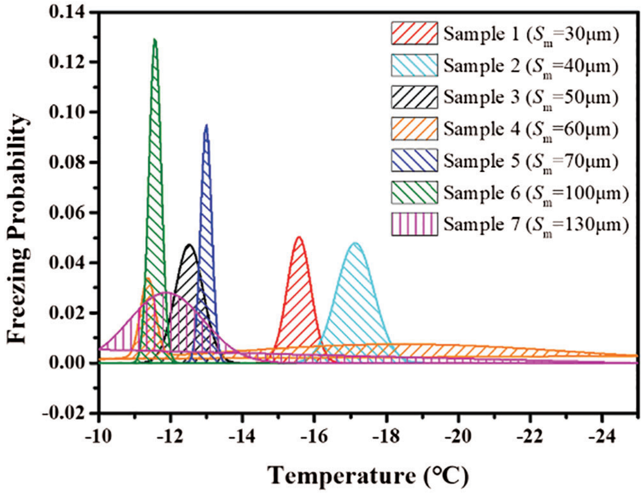

Figure 6: The Gaussian fitting curve of freezing probability distribution on the series of sample surfaces

From another perspective, the survival curve is defined as [38,39]:

$$F(T) = \frac{N(T)}{cN_0} \tag{3}$$

where F(T) reflects the relationship between temperature T and fraction of unfrozen events, c is the cooling rate, and N(T) is the number of unfrozen events. As shown in Fig. 7a, the survival curves for all these samples well conform to the typical characteristics on the crystal nucleation. The temperature for 50% unfrozen events is defined as the ice nucleation temperature, which is a statistical concept [40]. Obviously, the ice nucleation temperature can quantitatively reflect the ability of the micro-cubic structures inhibiting ice nucleation, and the results of ice nucleation temperature are in great agreement with the peak values of Gaussian fitting curves. The statistical analysis is an effective method to quantitatively analyze the ice nucleation behavior on the surface of the designed ice-repellent material.

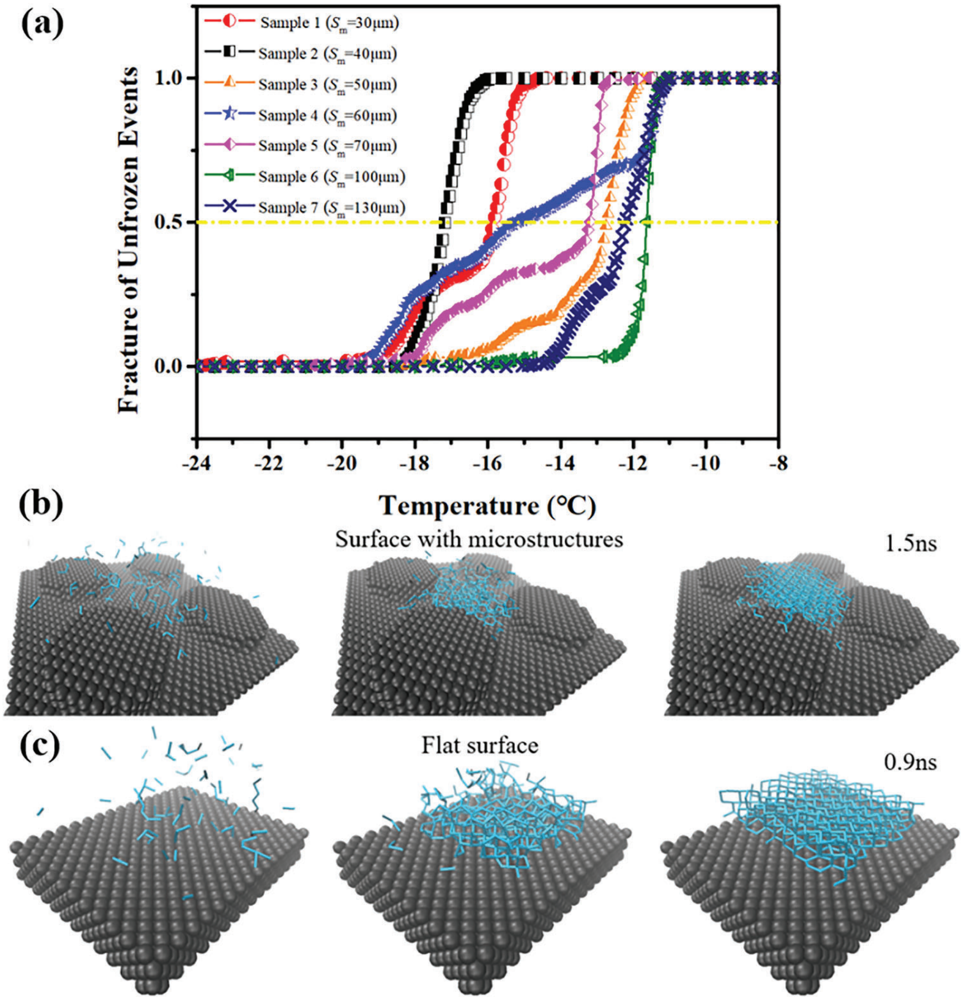

Figure 7: (a) The survival curves for all these samples, and the ice nucleation temperature with 50% unfrozen events; (b) Molecular dynamics simulation of ice nucleation on the surface with microscopic structures; (c) Molecular dynamics simulation of ice nucleation on flat surface

Furthermore, the molecular dynamic simulation results of water molecules changing into ice are shown in Figs. 7b and 7c, and further reveal the effect of surface microscopic structure configuration on the ice nucleation behavior. On the flat surface, ice crystal is disordered stacking structure without orientation, as shown in Fig. 7c. However, ice crystal is more likely to condense in the interval between the microscopic structures on the surface, as shown in Fig. 7b, finally causing longer ice nucleation time. The results well verify the decisive influence of interface wetting state on ice nucleation in the perspective of nanoscale.

3.4 Ice Nucleation Rate

Ice nucleation rate is the significant characterization parameter of ice nucleation, which can also be calculated by classical nucleation theory. All these samples have the same chemical composition. Therefore, the ice nucleation rate is mainly determined by microstructure configuration. To further investigate the effect of these microstructure configuration on ice nucleation rate, we assume that heterogeneous nucleation occurs at the water/silicon interface and the water droplet is 6 μL, whose schematic diagram is illustrated in Fig. 8a.

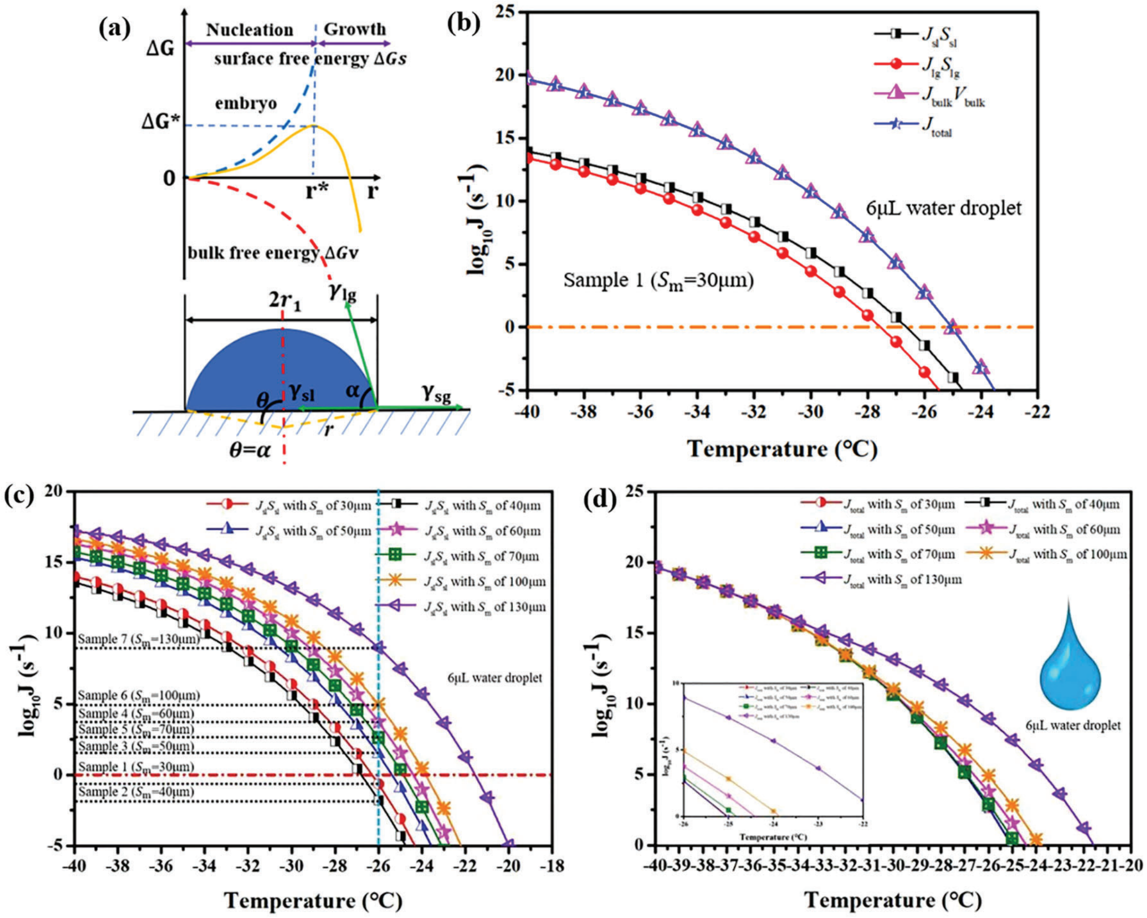

Figure 8: (a) Schematic diagram of heterogeneous nucleation barrier; (b) Bulk, liquid-gas, solid-liquid, and total ice nucleation rates on Sample 1 surface with micro-spacing distance of 30 μm; (c) Solid-liquid interface ice nucleation rate and (d) total ice nucleation rate on the serie of samples surfaces

According to classical nucleation theory, the solid-liquid interface nucleation rate can be expressed as [41]:

$$J_{sl}(T) = n \times \frac{kT}{h} \exp\left[-\frac{\Delta Q_{diff}(T)}{kT}\right] \exp\left[-\frac{\Delta G^{*}(T) f(\theta, T)}{kT}\right] \tag{4}$$

where n is the molecular surface density of water (≈1019 cm^{-2}), k is the Boltzman constant with 1.38×10^{-23} J/K, h is Planck constant with 6.626×10^{-34} J·s, $\Delta Q_{diff}(T)$ is the diffusion activation energy at certain temperature, $\Delta G^{*}(T)$ is the critical Gibbs free energy, and $f(\theta, T)$ is the wetting parameter at a certain temperature. These parameters are given by [42,43]:

$$\Delta Q_{diff}(T) = \frac{kT^2 E}{(T - T_0)^2} \tag{5}$$

$$\Delta G^{*}(T) = \frac{16\pi}{3} \frac{\gamma^3 {T_m}^2}{{\Delta H_{m,v}}^2 (T_m - T)} \tag{6}$$

$$f(\theta) = \frac{1}{4}(2 + cos\theta)(1 - cos\theta)^2 \tag{7}$$

where T_0 = 118 K and E = 892 K the fitting parameters [44], T_m is the melting point of water droplet with 273.15 K, $\Delta H_{m,v}$ is the latent heat of fusion with 3.06 × 108 J/m^{-3}, $\gamma = [28 + 0.25_{(T=273.15)}] \times 10^{-3}$ J/m^{-2} is the interface energy between ice and water [45,46], and θ is the WCA at certain temperature. Furthermore, the bulk nucleation rate can be written as [41]:

$$J_{bulk}(T) = n' \times \frac{kT}{h} \exp\left[-\frac{\Delta Q_{diff}(T)}{kT}\right] \exp\left[-\frac{\Delta G^{*}(T)}{kT}\right] \tag{8}$$

where n' is the molecular volume density of water with 3.1 × 1028 m^{-3}. Since the homogeneous nucleation occurs on liquid-gas contact interface, the liquid-gas nucleation rate and total nucleation can be expressed as [41,47,48]:

$$J_{lg}(T) = \frac{n}{n'} J_{bulk}(T) \tag{9}$$

$$J_{total}(T) = J_{sl}(T) S_{sl} + J_{lg}(T) S_{lg} + J_{bulk}(T) V \tag{10}$$

where $S_{sl} = \pi {r_1}^2$ the apparent solid-liquid contact area, $r_1 = \sqrt[3]{\frac{3V}{4\pi}} sin\theta$ is the radius of the apparent solid-liquid contact area, $S_{lg} = 4\pi r^2$ is the liquid-gas contact area, $r = \frac{r_1}{sin\theta}$ is the radius of the water droplet, and V is the volume of water droplet. The nucleation rate was calculated to further analyze the ice nucleation behavior on the serie of sample surfaces [49]. The Bulk, liquid-gas, solid-liquid, and total ice nucleation rates on Sample 1 with micro-spacing distance of 30 μm are calculated, as shown in Fig. 8b. Due to the corresponding change trend among the Bulk, liquid-gas, solid-liquid, and total ice nucleation rates is almost in a line, so that the other calculated results are not shows individually.

The surface microstructure configuration mainly produces a certain effect on the solid-liquid interface ice nucleation, and the solid-liquid interface ice nucleation rate $J_{sl}(T)$ is also calculated and shown in Fig. 8c. It is obvious that the $J_{sl}(T)$ on Sample 2 is less than that of Sample 1. This is mainly attributed to the relationship that the solid-liquid interface actual contact area S_{sl} on Sample 1 is ~1.78 times larger than that of Sample 2 under the same Cassie-Baxter wetting state. Larger S_{sl} of Sample 1 can greatly reduce the surface nuclear-shaped barrier, leading to smaller $J_{sl}(T)$. However, the other samples (i.e., Sample 3–7) well conforming to Wenzel wetting model also exhibit the corresponding trend with the value of S_{sl}. As for total ice nucleation rate, it is mainly governed by the Bulk ice nucleation rate

$J_{\mathrm{bulk}}(T)$, which is ~6 orders of magnitude higher than the $J_{\mathrm{sl}}(T)$, as shown in Fig. 8b. In consequence, all these samples exhibit the almost equal value to total ice nucleation rate, except Sample 7 with enough large S_{sl}.

4 Conclusions

In conclusion, we prepared a group of micro-cubic array structures on silicon sample surface by a selective plasma etching technique, and statistically explored the heterogeneous ice nucleation behavior. The as-constructed micro-cubic array structure surfaces also exhibited higher non-wettability with the water contact angle being up to 150°. On this basis, 500 cycles of freezing and melting processes were accurately recorded to analyze the instantaneous ice nucleation *via* the statistical results on freezing temperature. As a consequence, the micro-cubic array structures with the micro-spacing distance of 40 μm needed higher supercooling degree to induce the occurrence of ice nucleation, resulting in lower expectation temperatures of −17.13°C for the maximum freezing probability. This is due to higher stability of Cassie-Baxter wetting state on the sample surface with smaller micro-spacing distance. Furthermore, the gradually increasing micro-spacing distance to 60 μm would induce the transition from Cassie-Baxter wetting state to Wenzel wetting state, leading to higher freezing probability. Finally, this conclusion was well verified by the calculated ice nucleation rate based on the classical nucleation theory. This work will promote the mechanism understanding of surface microstructure configuration impeding heterogeneous ice nucleation for the design and construction of ideal icephobic materials.

Acknowledgement: The authors thank Prof. Jie Tao for the guidance of the molecular dynamics simulation.

Funding Statement: This work was supported by the National Natural Science Foundation of China (No. 51671105, 51705244), Natural Science Foundation of Jiangsu Province (No. BK20170790), the Project Funded by China Postdoctoral Science Foundation (No. 2019M661826), Fund of State Key Laboratory of Aerodynamics (SKLA2019020401), and Open Fund of Key Laboratory of Icing and Anti/De-icing (No. IADL20190202).

Conflicts of Interest: The authors declare that they have no conflicts of interest to report regarding the present study.

References

1. Zhu, K., Li, X., Su, J., Li, H., Zhao, Y. et al. (2018). Improvement of anti-icing properties of low surface energy coatings by introducing phase-change microcapsules. *Polymer Engineering & Science, 58(6),* 973–979. DOI 10.1002/pen.24654.
2. Zhang, S., Huang, J., Chen, Z., Yang, S., Lai, Y. (2019). Liquid mobility on superwettable surfaces for applications in energy and the environment. *Journal of Materials Chemistry A, 7(1),* 38–63. DOI 10.1039/C8TA09403A.
3. Kreder, M. J., Alvarenga, J., Kim, P., Aizenberg, J. (2016). Design of anti-icing surfaces: Smooth, textured or slippery? *Nature Reviews Materials, 7(1),* 15003. DOI 10.1038/natrevmats.2015.3.
4. Wang, T., Zheng, Y., Raji, A. R. O., Li, Y. Sikkema, W. K. A. et al. (2016). Passive anti-icing and active deicing films. *ACS Applied Materials & Interfaces, 8(22),* 14169–14173. DOI 10.1021/acsami.6b03060.
5. Huang, Z., Quan, Y., Mao, J., Wang, Y., Lai, Y. et al. (2019). Multifunctional superhydrophobic composite materials with remarkable mechanochemical robustness, stain repellency, oil-water separation and sound-absorption properties. *Chemical Engineering Journal, 358,* 1610–1619. DOI 10.1016/j.cej.2018.10.123.
6. Cheng, Y. T., Rodak, D. E. (2005). Is the lotus leaf superhydrophobic? *Applied Physics Letters, 86(14),* 144101. DOI 10.1063/1.1895487.
7. Zorba, V., Stratakis, E., Barberoglou, M., Spanakis, E., Tzanetakis, P. et al. (2008). Biomimetic artificial surfaces quantitatively reproduce the water repellency of a lotus leaf. *Advanced Materials, 20(21),* 4049–4054. DOI 10.1002/adma.200800651.

8. Ensikat, H. J., Ditsche-Kuru, P., Neinhuis, C., Barthlott, W. (2011). Superhydrophobicity in perfection: The outstanding properties of the lotus leaf. *Beilstein Journal of Nanotechnology, 2,* 152–161. DOI 10.3762/bjnano.2.19.
9. Cheng, Y., Zhu, T., Li, S., Huang, J., Mao, J. (2019). A novel strategy for fabricating robust superhydrophobic fabrics by environmentally-friendly enzyme etching. *Chemical Engineering Journal, 355,* 290–298. DOI 10.1016/j.cej.2018.08.113.
10. Varanasi, K. K., Deng, T., Smith, J. D., Hsu, M., Bhate, N. (2010). Frost formation and ice adhesion on superhydrophobic surfaces. *Applied Physics Letters, 97(23),* 234102. DOI 10.1063/1.3524513.
11. Zou, M., Beckford, S., Wei, R., Ellis, C., Hatton, G. et al. (2011). Effects of surface roughness and energy on ice adhesion strength. *Applied Surface Science, 257(8),* 3786–3792. DOI 10.1016/j.apsusc.2010.11.149.
12. Zhang, S., Huang, J., Cheng, Y., Yang, H., Chen, Z. et al. (2017). Bioinspired surfaces with superwettability for anti-icing and ice-phobic application: Concept, mechanism, and design. *Small, 13(48),* 1701867. DOI 10.1002/smll.201701867.
13. Bormashenko, E., Pogreb, R., Whyman, G., Erlich, M. (2007). Cassie–Wenzel transition in vibrating drops deposited on rough surfaces: Is the Dynamic Cassie-Wenzel wetting transition a 2D or 1D affair? *Langmuir, 23 (12),* 6501–6503. DOI 10.1021/la700935x.
14. Zhu, T., Cheng, Y., Cao, C., Mao, J., Lai, Y. (2020). A semi-interpenetrating network ionic hydrogel for strain sensing with high sensitivity, large strain range, and stable cycle performance. *Chemical Engineering Journal, 385,* 123912. DOI 10.1016/j.cej.2019.123912.
15. Suzuki, S., Nakajima, A., Yoshida, N., Sakai, M., Hashimoto, A. et al. (2007). Freezing of water droplets on silicon surfaces coated with various silanes. *Chemical Physics Letters, 445(1–3),* 37–41. DOI 10.1016/j.cplett.2007.07.066.
16. Gurganus, C. W., Charnawskas, J. C., Kostinski, A. B., Shaw, R. A. (2014). Nucleation at the contact line observed on nanotextured surfaces. *Physical Review Letters, 113(23),* 235701. DOI 10.1103/PhysRevLett.113.235701.
17. Lupi, L., Hudait, A., Molinero, V. (2014). Heterogeneous nucleation of ice on carbon surfaces. *Journal of the American Chemical Society, 136(8),* 3156–3164. DOI 10.1021/ja411507a.
18. Bi, Y., Cao, B., Li, T. (2017). Enhanced heterogeneous ice nucleation by special surface geometry. *Nature Communications, 8(1),* 15372. DOI 10.1038/ncomms15372.
19. Prestipino, S. (2018). The barrier to ice nucleation in monatomic water. *Journal of Chemical Physics, 148(12),* 124505. DOI 10.1063/1.5016518.
20. Yan, W., Cao, X., Tian, J., Jin, C., Ke, K. et al. (2016). Nitrogen/sulfur dual-doped 3D reduced graphene oxide networks-supported $CoFe_2O_4$ with enhanced electrocatalytic activities for oxygen reduction and evolution reactions. *Carbon, 99,* 195–202. DOI 10.1016/j.carbon.2015.12.011.
21. Chen, L., Guo, Z., Liu, W. (2016). Biomimetic multi-functional superamphiphobic FOTS-TiO_2 particles beyond lotus leaf. *ACS Applied Materials & Interfaces, 8(40),* 27188–27198. DOI 10.1021/acsami.6b06772.
22. Wu, S. Q., Wang, J. W., Shao, J., Wei, L., Yang, K. et al. (2017). Building a novel chemically modified polyaniline/thermally reduced graphene oxide hybrid through π-π interaction for fabricating acrylic resin elastomer-based composites with enhanced dielectric property. *ACS Applied Materials & Interfaces, 9(34),* 28887–28901. DOI 10.1021/acsami.7b07785.
23. Murakami, D., Jinnai, H., Takahara, A. (2014). Wetting transition from the Cassie–Baxter state to the Wenzel state on textured polymer surfaces. *Langmuir, 30(8),* 2061–2067. DOI 10.1021/la4049067.
24. Giacomello, A., Chinappi, M., Meloni, S., Casciola, C. M. (2012). Metastable wetting on superhydrophobic surfaces: Continuum and atomistic views of the Cassie-Baxter–Wenzel transition. *Physical Review Letters, 109 (22),* 226102. DOI 10.1103/PhysRevLett.109.226102.
25. Lin, Y., Chen, H., Wang, G., Liu, A. (2018). Recent progress in preparation and anti-icing applications of superhydrophobic coatings. *Coatings, 8(6),* 208. DOI 10.3390/coatings8060208.
26. Liu, Y., Li, X., Jin, J., Liu, J., Yan, Y. et al. (2016). Anti-icing property of bio-inspired micro-structure superhydrophobic surfaces and heat transfer model. *Applied Surface Science, 400,* 498–505. DOI 10.1016/j.apsusc.2016.12.219.

27. Zhu, C., Liu, S., Shen, Y., Tao, J., Pan, L. (2017). Verifying the deicing capacity of superhydrophobic anti-icing surfaces based on wind and thermal fields. *Surface and Coatings Technology, 309,* 703–708. DOI 10.1016/j.surfcoat.2016.10.098.
28. Shen, Y., Wang, G., Tao, J., Zhu, C., Liu, S. et al. (2017). Anti-icing performance of superhydrophobic texture surfaces depending on reference environments. *Advanced Materials Interfaces, 4(22),* 1700836. DOI 10.1002/admi.201700836.
29. Pan, S., Wang, N., Xiong, D., Deng, Y., Shi, Y. (2016). Fabrication of superhydrophobic coating via spraying method and its applications in anti-icing and anti-corrosion. *Applied Surface Science, 389,* 547–553. DOI 10.1016/j.apsusc.2016.07.138.
30. Jo, H. J., Ahn, H. S., Kang, S. H., Kim, M. H. (2011). A study of nucleate boiling heat transfer on hydrophilic, hydrophobic and heterogeneous wetting surfaces. *International Journal of Heat and Mass Transfer, 54(25–26),* 5643–5652. DOI 10.1016/j.ijheatmasstransfer.2011.06.001.
31. Gorobets, V., Bohdan, Y., Trokhaniak, V., Antypov, I. (2019). Investigations of heat transfer and hydrodynamics in heat exchangers with compact arrangements of tubes. *Applied Thermal Engineering, 151,* 46–54. DOI 10.1016/j.applthermaleng.2019.01.059.
32. Wilson, P. W., Lu, W., Xu, H., Kim, P., Kreder, M. J. et al. (2013). Inhibition of ice nucleation by slippery liquid-infused porous surfaces (SLIPS). *Physical Chemistry Chemical Physics, 15(2),* 581–585. DOI 10.1039/C2CP43586A.
33. Seeley, L. H., Seidler, G. T. (2001). Two-dimensional nucleation of ice from supercooled water. *Physical Review Letters, 87(5),* 055702. DOI 10.1103/PhysRevLett.87.055702.
34. Shaw, R. A., Durant, A. J., Mi, Y. (2005). Heterogeneous surface crystallization observed in undercooled water. *Journal of Physical Chemistry B, 109(20),* 9865–9868. DOI 10.1021/jp0506336.
35. Liu, C., Zheng, D., Zhao, L., Liu, C. (2014). Gaussian fitting for carotid and radial artery pressure waveforms: Comparison between normal subjects and heart failure patients. *Bio-Medical Materials and Engineering, 24(1),* 271–277. DOI 10.3233/BME-130808.
36. Lamraoui, F., Fortin, G., Benoit, R., Perron, J., Masson, C. (2014). Atmospheric icing impact on wind turbine production. *Cold Regions Science and Technology, 100,* 36–49. DOI 10.1016/j.coldregions.2013.12.008.
37. Zhang, C., Liu, H. (2016). Effect of drop size on the impact thermodynamics for supercooled large droplet in aircraft icing. *Physics of Fluids, 28(6),* 062107. DOI 10.1063/1.4953411.
38. Duft, D., Leisner, T. (2004). Laboratory evidence for volume-dominated nucleation of ice in supercooled water microdroplets. *Atmospheric Chemistry and Physics, 4(7),* 1997–2000. DOI 10.5194/acp-4-1997-2004.
39. Wilson, P. W., Heneghan, A. F., Haymet, A. D. J. (2003). Ice nucleation in nature: Supercooling point (SCP) measurements and the role of heterogeneous nucleation. *Cryobiology, 46(1),* 88–98. DOI 10.1016/S0011-2240(02)00182-7.
40. Whale, T. F., Murray, B. J., O'Sullivan, D., Umo, N. S., Morris, G. J. (2015). A technique for quantifying heterogeneous ice nucleation in microlitre supercooled water droplets. *Atmospheric Measurement Techniques, 8(6),* 2437–2447. DOI 10.5194/amt-8-2437-2015.
41. Wilson, P. W., Osterday, K. E., Heneghan, A. F., Haymet, A. D. J. (2010). Type I antifreeze proteins enhance ice nucleation above certain concentrations. *Journal of Biological Chemistry, 285(45),* 34741–34745. DOI 10.1074/jbc.M110.171983.
42. Rykaczewski, K., Anand, S., Subramanyam, S. B., Varanasi, K. K. (2013). Mechanism of frost formation on lubricant-impregnated surfaces. *Langmuir, 29(17),* 5230–5238. DOI 10.1021/la400801s.
43. Hao, P., Lv, C., Zhang, X. (2014). Freezing of sessile water droplets on surfaces with various roughness and wettability. *Applied Physics Letters, 104(16),* 161609. DOI 10.1063/1.4873345.
44. Zhang, Z., Liu, X. Y. (2018). Control of ice nucleation: Freezing and antifreeze strategies. *Chemical Society Reviews, 47(18),* 7116–7139. DOI 10.1039/C8CS00626A.
45. Smith, R. S., Kay, B. D. (1999). The existence of supercooled liquid water at 150 K. *Nature, 398(6730),* 788–791. DOI 10.1038/19725.

46. Fu, Q. T., Liu, E. J., Wilson, P., Chen, Z. (2015). Ice nucleation behaviour on sol–gel coatings with different surface energy and roughness. *Physical Chemistry Chemical Physics, 17(33),* 21492–21500. DOI 10.1039/C5CP03243A.
47. Johari, G. P. (1997). The Gibbs–Thomson effect and intergranular melting in ice emulsions: Interpreting the anomalous heat capacity and volume of supercooled water. *Journal of Chemical Physics, 107(23),* 10154–10165. DOI 10.1063/1.475322.
48. Alizadeh, A., Yamada, M., Li, R., Shang, W., Otta, S. et al. (2012). Dynamics of ice nucleation on water repellent surfaces. *Langmuir, 28(6),* 3180–3186. DOI 10.1021/la2045256.
49. Zobrist, B., Koop, T., Luo, B. P., Marcolli, C., Peter, T. (2007). Heterogeneous ice nucleation rate coefficient of water droplets coated by a nonadecanol monolayer. *Journal of Physical Chemistry C, 111(5),* 2149–2155. DOI 10.1021/jp066080w.